Activation of the type 3 secretion system of enteropathogenic *E. coli* leads to reprogramming of its lipid metabolism

Anish Zacharia[1], Ritesh Ranjan Pal[2,3], Naama Katsowich[2], Chanchal Thomas Mannully [1], Ayda Ibrahem[1], Sivan Alfandary[1], Raphael Serruya[1], Amit K Baidya[2], Sigal Ben-Yehuda[2], Ilan Rosenshine[2], Arieh Moussaieff[1]*

1. The Institute for Drug Research, The Hebrew University of Jerusalem, Jerusalem, Israel
2. Department of Microbiology and Molecular Genetics, Institute of Medical Research Israel-Canada, Faculty of Medicine, The Hebrew University of Jerusalem, Jerusalem, Israel
3. School of Biological Sciences, Indian Association for the Cultivation of Science, Kolkata, India

* For correspondence: ariehm@ekmd.huji.ac.il

Abstract

The type III secretion system (T3SS) is critical for the virulence of enteropathogenic *E. coli* (EPEC), an important human pathogen. T3SS is activated upon host attachment leading to effector injection, which is associated with repression of CsrA. CsrA repression results in gene expression reprogramming, which contributes to EPEC adaptation to a cell-adherent lifestyle. However, how this reprogramming influences EPEC physiology remains poorly understood. By combining genetic analyses, metabolomics and lipidomics, and data mining from reported datasets, we show that activation of the EPEC T3SS is associated with massive metabolic shifts, in particular, remodeling of lipid metabolism. The latter includes a shift from phospholipids towards lysophospholipids and cardiolipins and from ubiquinones and menaquinones production to the synthesis of undecaprenyl isoprenoids, concomitant to upregulation of O-antigen biosynthesis. We predict that the lipid remodeling upon attachment to host cells and T3SS activation contributes to bacterial fitness and promote host colonization.

Introduction

Enteropathogenic *E. coli* (EPEC) is a common cause of pediatric diarrhea (1). Upon attachment to the host intestinal epithelium, this pathogen employs a type 3 secretion system (T3SS) to inject effector proteins into the host cells. The T3SS is encoded within a pathogenicity island termed the locus of enterocyte effacement (LEE) (2), composed of a cluster of transcriptional units containing 41 genes encoding for T3SS structural components, six translocated effectors, and related proteins (3, 4). The LEE5 operon contains three genes: *tir*, *cesT*, and *eae*, encoding Tir, CesT, and intimin, respectively (5, 6). Tir (Translocated intimin receptor) is the most abundant effector and the first to be translocated into the host cell (7, 8). CesT is a homodimer chaperone associated with many effectors, of which Tir is the major one (9, 10). CesT binds to two regions in Tir at the N- and C-terminus through a specific recognition motif, promoting Tir stability and its translocation to the host (9). Immediately following its translocation into the host, Tir is targeted to the host cell membrane and becomes an integral membrane protein with two transmembrane domains and a surface-exposed loop. Intimin, the third product of the LEE5 operon, is an outer membrane protein that promotes adherence of EPEC to the host via interaction with the surface exposed loop of translocated Tir (11, 12). This attachment type was termed intimate attachment (11).

CesT-Tir interaction is essential for Tir translocation into the host and the subsequent intimate attachment action. The second function of CesT-Tir interaction is related to the rearrangement of gene expression upon EPEC-host contact and the consequent Tir translocation (13). In planktonic EPEC, CesT remains bound to Tir and other effectors and the T3SS is not active but fully assembled, ready to immediately translate the effectors upon contact with the host cell. Upon bacteria-host contact, the T3SS is activated, followed by immediate and rapid delivery of Tir and other effectors into the host cell (8, 9, 14, 15). The delivery of these effectors into the host liberates CesT resulting in increased levels of free CesT in the EPEC cytoplasm. The liberated CesT then interacts with an alternative binding partner, the carbon storage regulator A (CsrA) (9, 13, 16). CsrA is an RNA-binding protein and posttranscriptional regulator, which coordinates numerous bacteria functions, including motility, metabolism, and virulence (17, 18). Notably, the elevated levels of free CesT, upon effectors injection, competitively inhibit CsrA-mRNA interaction. Since CsrA binds to the mRNA of numerous genes and regulates the stability and/or translation of these mRNAs, CesT-CsrA interaction and the consequential liberation of the mRNAs result in massive remodeling of gene expression (**Figure 1**).

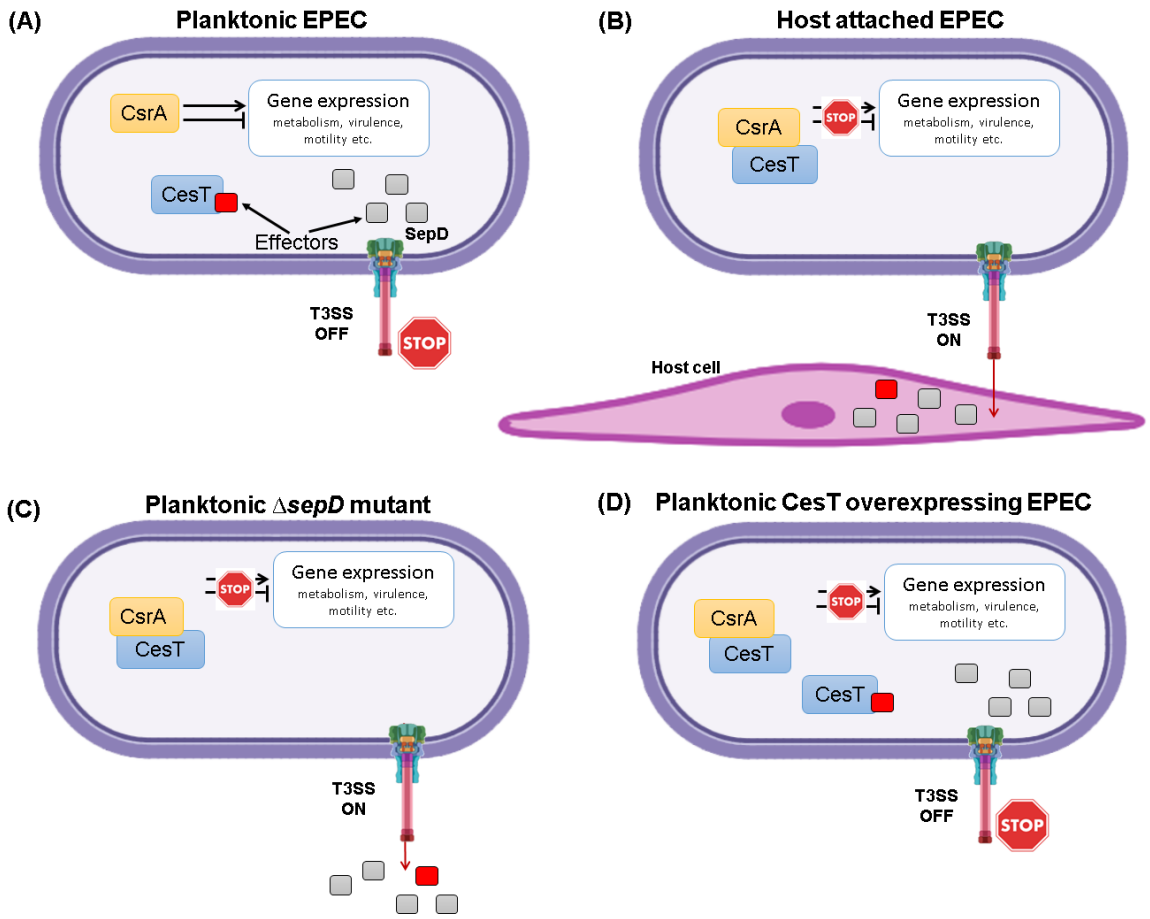

Figure 1. A scheme of the T3SS regulation of EPEC attachment to the host cell.

(A) Planktonic EPEC: The T3SS is not active (OFF). The effectors accumulate in the cytoplasm, and some of them (indicated as a red square) bind to CesT and sequester it. In these bacteria, CsrA is free to bind mRNA and regulate, mostly repress, gene expression.

(B) Host-attached EPEC: The T3SS is activated upon contact with the host, eliminating the effectors from the EPEC cytoplasm by injecting them into the host cell. The liberated CesT then binds to CsrA to inhibit CsrA-mRNA interaction.

(C) Planktonic Δ*sepD* mutant: The T3SS is constitutively active, and effectors are secreted. The liberated CesT binds to CsrA and inhibits CsrA-mRNA interaction.

(D) Planktonic CesT overexpressing EPEC: CesT is expressed at levels that allow binding to all the CesT-binding effectors and CsrA, resulting in inhibition of CsrA-mRNA interactions regardless of the T3SS activity.

The significance of the CesT-CsrA switch to the bacterial physiology can be partially extrapolated from studies comparing wild type *E. coli* to the *csrA* mutant with null or residual activity (17, 19-24). However, *csrA* mutants are not the ideal model to mimic host interacting EPEC since the CesT-CsrA interaction induces only partial and temporal CsrA inhibition. Previous reports point to alternative approaches that better mimic the physiological state of host-attached EPEC. The first approach employs the EPEC *sepD* mutant (Δ*sepD*), which expresses T3SS that constitutively secretes Tir regardless to host attachment (13, 25). Thus, the *sepD* mutant contains higher levels of liberated CesT that is free to interact with CsrA. Another approach uses wild-type EPEC containing a plasmid that expresses CesT under an IPTG regulated promoter (EPEC/pCesT). This strain may be induced to transiently overexpress CesT upon IPTG treatment to make in the bacteria a sufficient amount of free CesT, that readily interacts with CsrA (**Figure 1**).

Here, we combined metabolomics and genetic methodologies to characterize the shift of EPEC metabolism under conditions that mimic attachment to the host cell and the associated CsrA inhibition. Surprisingly, our unbiased metabolomics analyses pointed to alterations in the lipid composition as a major metabolic signature of this shift. We expect this lipid shift to be a universal trait in the *E. coli* spp. when experiencing CsrA inhibition. We further assume that this lipidomic shift is involved in the adaptation of EPEC to a cell-adherent lifestyle.

Results

T3SS activity is associated with reprogramming of EPEC metabolism

We sought to unveil the metabolic shifts that take place in EPEC upon T3SS activation and effector injection. However, obtaining biological material from injecting EPEC in quantities that allow metabolomics analysis is complicated, as one subpopulation is engaged in injection (8), while in the other subpopulation the T3SS remains inactive. To overcome this obstacle and obtain uniform populations, we grew the bacteria under conditions that promote the expression of the T3SS genes (i.e., growth in 500 ml DMEM, 37°C, without shaking). Using these growth conditions, we compared wild type EPEC that does not secrete Tir (thus Tir sequesters CesT), to an EPEC Δ*sepD* mutant that constitutively secretes Tir, and consequently, CesT is liberated, free to interact with CsrA. As a control, we used EPEC with a deleted *csrA* gene (Δ*csrA*). The latter was also used as a

reference to available data of the metabolic profile of the EPEC and E. coli K12 Δ*csrA* mutant (21, 24, 26).

Bacterial cultures were grown in DMEM without shaking to OD_{600} 0.6. Under our experimental conditions, Δ*csrA* strains showed attenuated growth rate (**Supplementary Figure 1)**, in line with previous literature (18, 21, 26), wheras other strains showed similar growth rate to the wild type. The Δ*sepD* Δ*cesT* showed a mild attenuation in growth rate. Upon reaching a density of OD_{600} 0.6, the cultures were harvested, metabolites were extracted, and an unbiased LC-MS-based metabolomics analysis was carried out. We performed preliminary analyses following extraction with several semi-polar solvent systems (27) and then carried out a global metabolomics analysis using an acetonitrile: methanol: water (40:40:20) solvent system. We detected 25,999 metabolic features. After the exclusion of possible artifact features (see Methods section), analysis was carried out using 5,790 mass features. Variable Importance in Projection (VIP) analysis revealed 41 differential metabolic features in the Δ*sepD* strain. Notably, out of the 41 differential lipids 14 were phospholipids (PLs) (**Supplementary Table 1**). These metabolic signatures were reiterated and emphasized in the *csrA* null mutant. Other notable metabolic signatures of the mutant strains included the decreased abundance of acetyl CoA and UDP glucose, and the upregulated levels of reduced glutathione, in contrast to the downregulation of oxidized glutathione (**Supplementary Table 1**). Taken together, our data suggest that the constitutive activity of the T3SS in both the *sepD* and the *csrA* mutants is similarly associated with a shift in lipid composition. These results corroborate the notion that the metabolic shift found in the *sepD* mutant is mediated by repression of CsrA, and suggest that they cause a shift in lipid metbaolism.

Alterations in phospholipid and terpenoid-quinones pathways mediated by CesT-CsrA interaction.

Since our untargeted metabolomics analyses suggested that T3SS activation leads to altered lipid metabolism, we next performed a lipidomics study. To mimic the attachement to host cells we studied the lipid composition of wild type EPEC, Δ*sepD* mutant, and wild type EPEC overexpressing recombinant CesT from a plasmid (EPEC/pCesT). These strains transiently and partially inhibit csrA (as in attached EPEC) and show a growth rate similar to that of the wild type EPEC in our experimental conditions.

A total of 15,827 mass features was detected. After the exclusion of possible artifact features (see Methods section), analysis was carried out using 3,277 mass features. Principal component analysis (PCA) demonstrated a striking separation between the lipidome of the Δ*sepD* mutant and that of wild type EPEC, with PC1 accounting for 97.9% of the variance (**Figure 2A**). These results suggest that the increased levels of free CesT in the Δ*sepD* mutant induced the observed metabolic shift. To test this hypothesis, we added to our analysis a mutant deleted of both *sepD* and *cesT* (Δ*sepD* Δ*cesT*). Indeed, the PCA of the lipidome of the strains examined showed no shift in the lipid composition in the absence of CesT (**Figure 2B**). To further confirm that the increased levels of free CesT are responsible for the lipid shift, we overexpressed free CesT in EPEC/pCesT. The overexpression of CesT was sufficient for inducing the shift in lipid composition (**Figure 2B**). Taken together, our data suggest that an increase in the levels of CesT is necessary and sufficient to induce a considerable shift in the lipid composition of EPEC. A VIP analysis of Δ*sepD* vs. wild type EPEC lipidome revealed 54 mass features. PLs and isoprenoids of the quinone terpenoid subclass were major groups of differential lipids (**Figure 2C**). We then identified lipids of the two main differential classes: 111 PLs, and 70 terpenoids, and performed PCAs of the identified species of each of the two lipid classes. We found a distinct separation of the lipids in both subclasses (**Figure 2D-G**), in the *sepD* mutants (**Figure 2D,F**) and EPEC/pCesT (**Figure 2E,G**). We thus focused our analyses thereof on the terpenoid-quinones isoprenoid and phospholipid pathways.

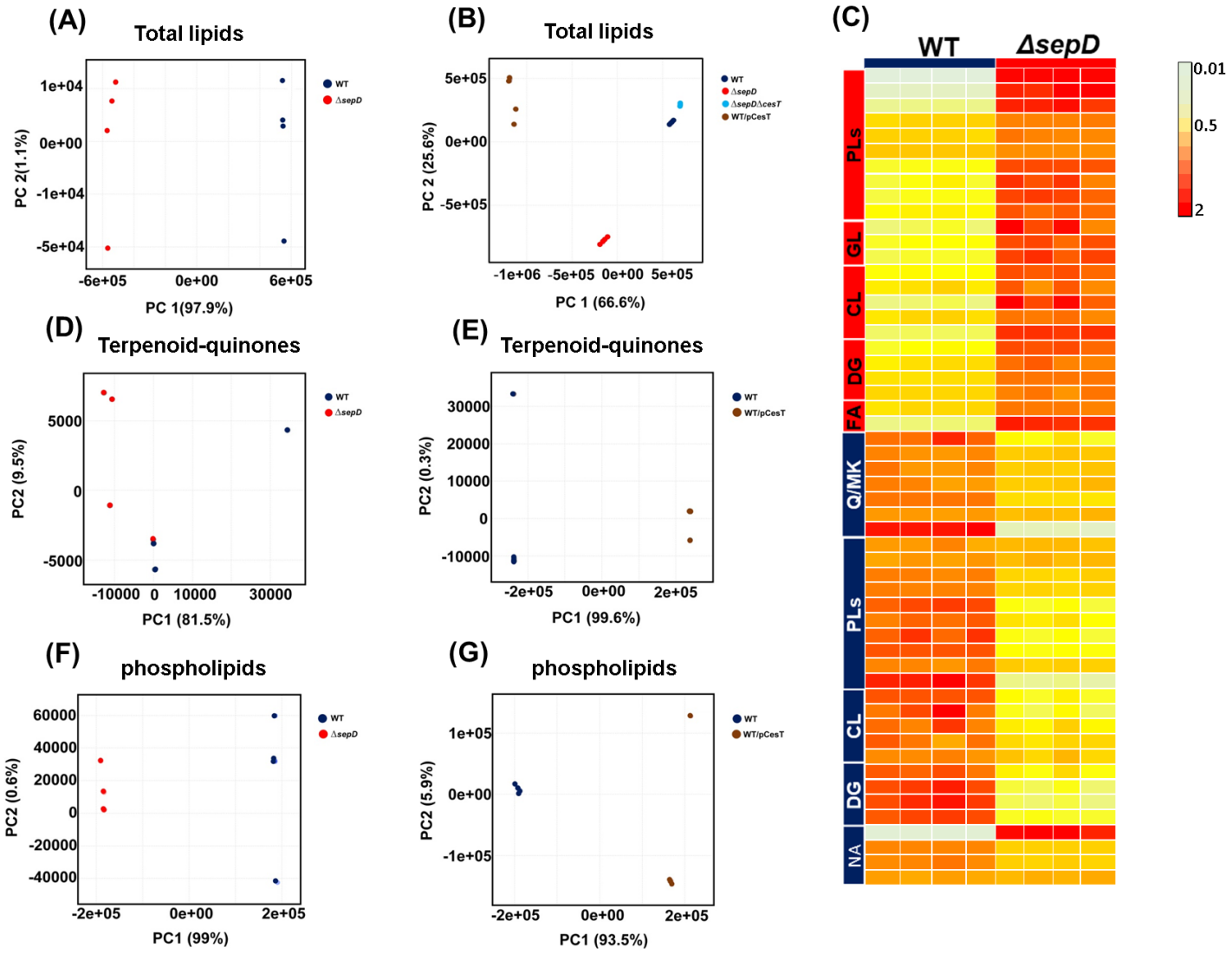

Figure 2. T3SS exerts a profound effect on *E. coli* lipid metabolism. (A-C) The lipidome of EPEC T3SS mutants is fully separated from that of the wild type strain (WT). Principal component analysis (PCA) of *sepD* mutant EPEC vs. WT (A). (B) PCA of Δ*sepD*, pCesT, and rescue of the lipid phenotype in the *sepD cesT* double mutant. (C) A heat map of the differential lipids (Variable Importance in Projection (VIP) >1) in *sepD* mutants divided into lipid subclasses. Lipid classes with upregulated accumulation in mutants are in red, and lipid classes with downregulated accumulation in mutants are in blue quadrants. (D-G) PCA analyses of lipid subclasses in the *sepD* mutants vs. the WT strain. (D-E) PCAs of terpenoid-quinones in WT vs. Δ*sepD* (D) or pCesT (E). (F-G) PCAs of phospholipids in WT vs. Δ*sepD* (F) or pCesT (G). N=4. GL, Glycolipids; CL, Cardiolipins; DG, Diglyceride/Diacyliglycerol; FA, Fatty acids; Q/MK-Ubiquinone/Menaquinone; PLs, Phospholipids.

Undecaprenyl lipid biosynthesis is upregulated, whereas synthesis of menaquinones and ubiquinones is downregulated upon T3SS activation.

To better understand the changes in EPEC isoprenoid metabolism following T3SS activation, we mined a database of gene expression alterations in *csrA E. coli* mutant (24). We found that the undecaprenyl branch of the terpenoid quinone pathway was upregulated in the *csrA* mutant, with no clear metabolic alterations in the menaquinone and ubiquinone branch (**Figure 3**).

To clarify the influence of CsrA on the menaquinone and ubiquinone branches of the isoprenoid pathway and to investigate possible post-translational effects of CsrA on lipid metabolism, we further mined a reported *E. coli* CsrA CLIP-seq dataset (17). The extracted data suggest potential post-translational regulation of the terpenoid quinone pathway by CsrA, including post-translational repression of menaquinone biosynthesis (**Supplementary Figure 2**).

We next compared the levels of isoprenoids in the Δ*sepD* EPEC to those of a wild type strain. In addition, to corroborate the T3SS-dependent lipid profile, and to exclude possible non-specific effects of the mutation, we studied the lipid composition upon CesT overexpression (EPEC/pCesT). We quantified the relative abundances of the identified isoprenoids per lipid subclasses. This analysis pointed to a shift from ubiquinone and menaquinone to undecaprenyl biosynthesis in the *sepD* mutants (**Figure 4A-D**). Notably, this shift was recapitulated and was, in fact, more pronounced in EPEC overexpressing CesT (**Figure 4A-D**).

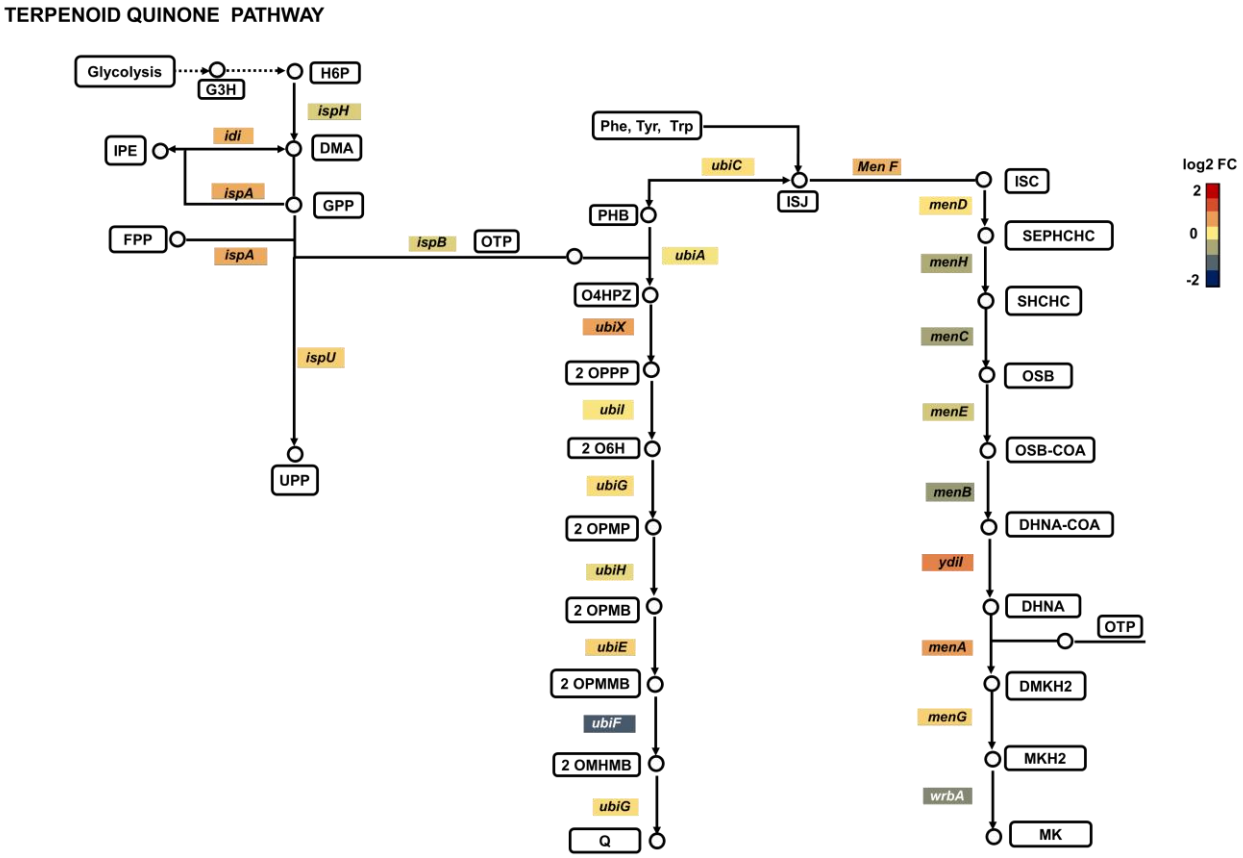

Figure 3. Data mining in the Δ*csrA* transcriptome (24) suggests upregulation of undecaprenyl biosynthesis. Network was adapted from Kyoto Encyclopedia of Genes and Genomes (KEGG) for Escherichia coli O127:H6 E2348/69 (EPEC), and modified to include undecaprenyl, ubiquinone and menaquinone branches of terpenoid pathway. Lipids are represented by circles, with their names in white quadrants. Enzyme are represented by arrows, with their names in colored . The color of quadrants represent the log fold change of the *csrA* mutant from the WT strain. H6P- 1-Hydroxy-2-methyl-2-butenyl- 4-diphosphate; DMA- Dimethylallyl diphosphate; IPE- Isopentenyl diphosphate; GPP- Geranyl diphosphate; FPP- Farnesyl diphosphate; UPP- Undecaprenyl diphosphate; OTP- Octaprenyldiphosphate; PHB- Hydroxybenzoic acid; ISJ- Chorismate; O4HPZ- 4-Hydroxy-3-polyprenyl benzoate; 2OPPP- 2-Octaprenyl phenol; 2O6H- 2-Octaprenyl-6-hydroxyphenol; 2OPMP- 2-Octaprenyl-6-methoxy phenol; 2OPMB- 2-Octaprenyl-6-methoxy-1,4-benzoquinone; 2OPMMB- 2-Octaprenyl-3-methyl-6-methoxy-1,4-benzoquinone; 2OMHMB- 2-Octaprenyl-3-methyl-5-hydroxy-6-methoxy-1,4-benzoquinone; Q- Ubiquinone; ISC- Isochorismate; SEPHCHC- 2-Succinyl-5-enolpyruvyl-6-hydroxy-3-cyclohexene-1-carboxylate; SHCHC-6-Hydroxy-2-succinylcyclohexa-2,4-diene-1carboxylate; OSB- 2-Succinylbenzoate; OSB-COA- 2-Succinylbenzoyl-CoA; DHNA-CoA- 1,4-Dihydroxy-2-naphthoyl-CoA; DHNA- 1,4-Dihydroxy-2-naphthoate; DMKH2- Demethylmenaquinol; MKH2- Menaquinol; MK- Menaquinone.

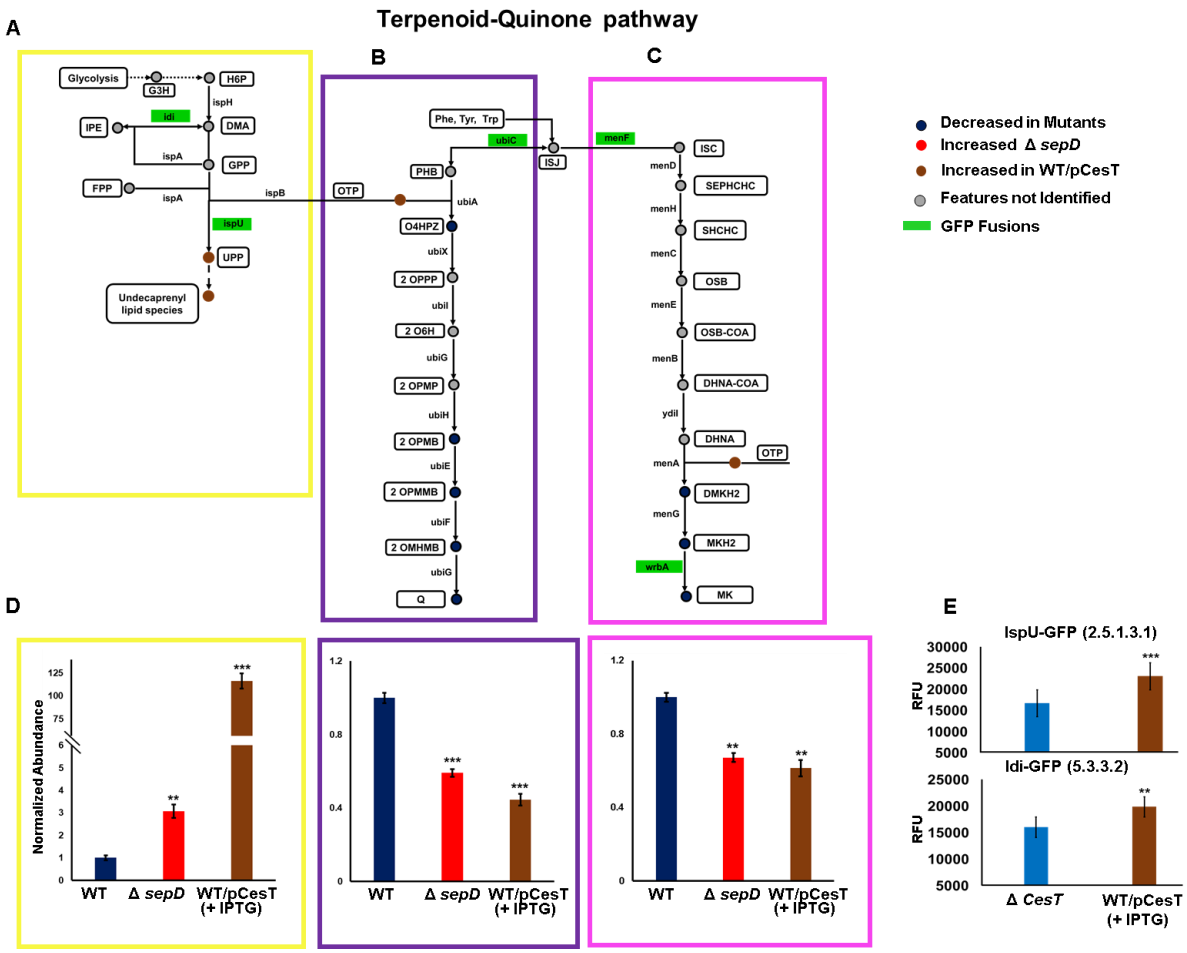

Figure 4. Activation of T3SS in EPEC upregulates the biosynthesis of undecaprenyl lipids and downregulates the biosynthesis of menaquinones and ubiquinones. Network was adapted from Kyoto Encyclopedia of Genes and Genomes (KEGG) for Escherichia coli O127:H6 E2348/69 (EPEC), and modified to include undecaprenyl, ubiquinone and menaquinone branches of terpenoid pathway. (A-C) A simplified scheme of the metabolic network of terpenoid quinone lipids, divided into undecaprenyl (yellow box), ubiquinone (purple box), and menaquinone (pink box). The colors of lipid species represent their relative accumulation according to our lipidomics analyses (in circles). Identified lipid species are in white boxes. Enzyme names are in an ellipse, and green boxes represent enzyes fused to GFP; their expression was determined in terms of relative fluorescence unit (RFU). (D) Accumulated normalized abundance of undecaprenyl lipids, ubiquinones, and menaquinones, respectively, in 'host cell attachment' like conditions. (E) Quantification of GFP fluorescence of enzymes involved in terpenoid-quinone biosynthesis in T3SS mutants. N=4 for A-D; N=3 and the average of 3 experiments is shown for E. Data are presented as mean ± SE. *, $p<0.05$; **, $p<0.01$; ***, $p<0.001$. H6P- 1-Hydroxy-2-methyl-2-butenyl- 4-diphosphate; DMA- Dimethylallyl diphosphate; IPE- Isopentenyl diphosphate; GPP- Geranyl diphosphate; FPP- Farnesyl diphosphate; UPP- Undecaprenyl diphosphate; OTP- Octaprenyldiphosphate; PHB- Hydroxybenzoic acid; ISJ- Chorismate; O4HPZ- 4-Hydroxy-3-polyprenyl benzoate; 2OPPP- 2-Octaprenyl phenol; 2O6H- 2-Octaprenyl-6-hydroxyphenol; 2OPMP- 2-Octaprenyl-6-methoxy phenol; 2OPMB- 2-Octaprenyl-6-methoxy-1,4-benzoquinone; 2OPMMB- 2-Octaprenyl-3-methyl-6-methoxy-1,4-benzoquinone; 2OMHMB- 2-Octaprenyl-3-methyl-5-hydroxy-6-methoxy-1,4-benzoquinone; Q- Ubiquinone; ISC- Isochorismate; SEPHCHC- 2-Succinyl-5-enolpyruvyl-6-hydroxy-3-cyclohexene-1-carboxylate; SHCHC- 6-Hydroxy-2-succinylcyclohexa-2,4-diene-1-carboxylate; OSB- 2-Succinylbenzoate; OSB-COA- 2-Succinylbenzoyl-CoA; DHNA-CoA- 1,4-Dihydroxy-2-naphthoyl-CoA; DHNA- 1,4-Dihydroxy-2-naphthoate; DMKH2- Demethylmenaquinol; MKH2- Menaquinol; MK- Menaquinone.

We then tested the influence of CesT levels on the production of enzymes involved in the terpenoid-quinones biosynthesis. To this end, we fused the *gfp* reporter gene in frame to the 3' end of a selected number of genes in their native chromosomal location without perturbing their regulatory regions. As parental strains, we used wild type EPEC or the Δ*cesT* mutant and selected genes involved in the isoprenoid pathway. Using this approach, we *gfp*-tagged the following genes: *idi*, which forms isopentenyl pyrophosphate - isoprenoid precursor, *ispU*, involved in the biosynthesis of undecaprenyl pyrophosphate, *ubiC* and *menF*, bridging between menaquinone and ubiquinone pathways, and *wrbA* encoding for the menaquinone enzyme. We then fluorometrically compared the GFP levels in bacteria lacking and overexpressing CesT in these strains. We detected significant upregulation of Idi-GFP and IspU-GFP upon CesT overexpression (**Figure 4E**). This increase is in agreement with the lipid accumulation that we measured. Changes in the levels of GFP-tagged enzymes involved in menaquinone and ubiquinone production were not significant (**Supplementary Fig 3**).

T3SS regulates phospholipid biosynthesis

A second, and very prominent differential lipid class we identified is PLs: the major lipid constituents of cellular membranes, providing a strong incentive to decipher the influence of T3SS activity on PL composition. We first quantified all identified PLs (**Figure 5A**) and found a mild but significant decrease in PL levels in the Δ*sepD* mutant, and upon CesT overexpression, concomitant with increased levels of cardiolipins (CLs; **Figure 5B**) and lysophospholipids (LPLs) (**Figure 5C**). These results suggest shifts from PLs towards CLs and LPLs. To better understand the changes in PL metabolism, we quantified the abundance of PL subclasses. Interestingly, we found lower abundance of phosphatidyl glycerols (PGs; **Figure 5D**) and phosphatidylserines (PS; **Figure 5E**) in the Δ*sepD* mutant and upon CesT overexpression, associated with a higher abundance of phosphatidyl ethanolamines (PEs; **Figure 5F**) and phosphatidic acids (PA; **Figure 5G**). The abundance of lysophosphatidic acids (LPAs), which form a group of signaling molecules of particular interest, was dramatically increased in the mutants (**Figure 5H**). This shift in PL composition towards LPLs was concomitant to a decrease in the abundance of identified PLs. The lower PL abundance was reflected by lower fluorescence intensity as a result of staining with lipophilic probe FM™ 4-64FX, binding to the outer leaf of the plasma membrane (**Figure 5I, 5J**).

We also noted a lower degree of unsaturation (DOU, generally representing the number of double bonds in PLs) of the PLs in the Δ*sepD* mutant and upon CesT overexpression (**Supplementary Figure 5A**), as well as a decreased chain length (**Supplementary Figure 5B**). For a complete picture of the T3SS-dependent lipid metabolism, we mined a *csrA*-mutant transcriptome database (24) for the glycerophospholipid pathway genes. We performed a network-based analysis that integrated our lipidomics data and the published gene expression data. Our network-based analysis was well-aligned with the results of our analyses of the abundance of PL subclasses (**Figure 5K**). Altogether, our analyses suggest that inhibition of CsrA by CesT leads to a shift from PS to PEs, PAs, and LPLs, and from PGs to CLs.

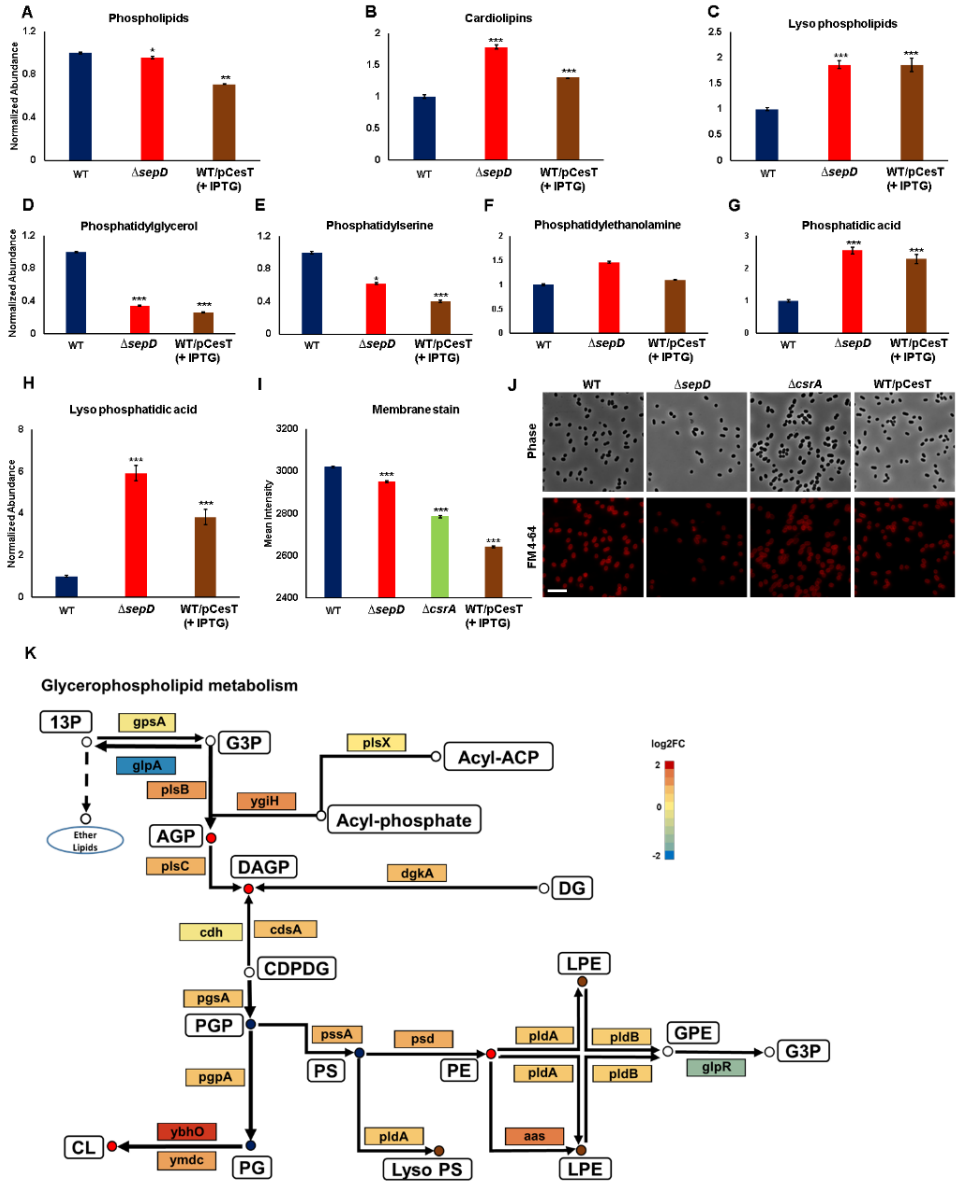

Figure 5. Inhibition of CsrA by CesT leads to a shift from PS to PEs, PAs, and LPLs, and from PGs to CLs. The abundance of phospholipids (A), cardiolipins (B), and lysophospholipids (C). (D-G) The abundance of phospholipid classes: phosphatidylglycerols (D), phosphatidylserines (E), phosphatidylethanolamines (F), phosphatidic acids (G), and lysophosphatidic acids (H). Membrane stain analysis showing the lower uptake of membrane stain FM 4-64 in the mutant strains (I). Phase-contrast and fluorescent images of EPEC WT and mutants upon FM 4-64 membrane staining (J). A metabolic map of phospholipids integrating our lipidomics data with the corresponding gene expression (given for the CsrA mutant), mined in (24) (K). Lipid classes are represented by circles, with their names in white quadrants. Enzymes are represented by arrows, with their names in colored quadrants. The color of circles (lipid classes) and quadrants (gene expression) are given as ln2 (fold change), relative to the wild type. 13P, Glycerone phosphate; G3P, Glycerol-3-phosphate; AGP, Acylglycerol-3-phosphate; DAGP, 1,2-Diacylglycerol 3-phosphate; CDPDG, 1,2-Diacylglycerol-cytidine 5-diphosphate; GPE, Glycerophosphoethanolamine; LPE, Lysophosophoethanolamine; Lyso Ps, Lysophosphoserine; PGP, Phosphatidylglycerophosphate; PE, Phosphatidylethanolamine; PS, Phosphatidylserine; PG, Phosphatidylglycerol; CL, Cardiolipins. Scale bar indicates 5 μm. N=4 for A-I and K; L represents the quantification of fluorescence emission from ~ 10,000 bacteria for each strain, in 3 technical replicates . Data are presented as mean ± SE. *, $p<0.05$; ***, $p<0.001$.

A previous study reported lower levels of LPLs in the Δ*csrA* strain compared to WT EPEC (24). The seeming discrepancy between our results and the previously published ones could be due to differences in the experimental conditions, such as the growth medium used, or differences in the methods used for sample preparation: we used a lipid extraction system, whereas Berndt and colleagues used an extraction system optimized for species with medium polarity. To examine the latter option, we quantified the LPLs found in the extraction system we used for global metabolomics (suited for the extraction of lipid species with medium polarity) and detected a similar increase in the abundance of LPLs to that found in our lipid extracts (**Supplementary Figure 4**).

Our analysis demonstrates increased accumulation of undecaprenyl species. Importantly, undecaprenylpyrophoshate (UPP), highly accumulated in the mutants, is responsible for trafficking the building units of lipopolysaccharides (LPS) across the membrane for the biosynthesis of LPS.

We used a LPS O-antigen labelling procedure to determine the levels of LPS O-antigen in EPEC. We noted a higher fluorescence intensity in the Δ*sepD* mutant and CesT overexpressing EPEC strains, representing the increased levels of LPS O-antigen **(Figure 6A-B)**.

We reasoned that the changes found in the composition of EPEC membrane lipids, particularly PLs, may be reflected in its physiological and morphological characteristics, such as cell size and cell surface area/volume ratio. Therefore, we measured the Δ*sepD* mutant and EPEC/pCesT and found a significant increase in their size (**Figure 7A**). Yet, the size of the *csrA* mutant was similar to that of wild type EPEC. Lipid composition may also influence cell surface charge, which may play roles in charge-dependent adhesion of bacteria to oppositely charged surfaces. We thus compared the Zeta potential of wild type EPEC to that of the mutants and found an increase in the negative charge of the mutant strains (**Figure 7B**).

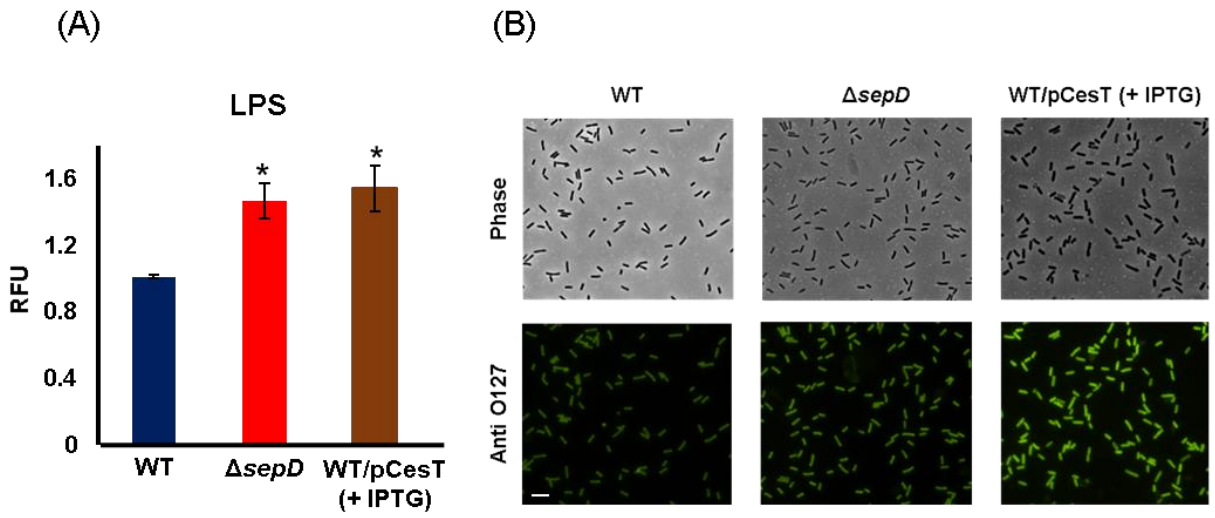

Figure 6. Lipopolysacharides levels in EPEC increase upon T3SS activation. Indicated EPEC strains were subcultured in DMEM at 37˚C to an OD_{600} of 0.6. The cells were fixed on the coverslip and incubated with rabbit anti-O127 antiserum. The labelling was done with Alexa 488 conjugated goat anti-rabbit antibody. Flourecence Images of EPEC strains were were visualized under phase contrast and flurescent optics using Eclipse Ti microscope and the relative fluorescence exhibited by the EPEC strains were determined using NIS Elements AR 4.3 (Nikon, Japan) (A-B). Scale bar indicates 5 µm. N=3 and ~ 700 bacteria per strain. Data are presented as mean ± SE. *, $p<0.05$; ***, $p<0.001$.

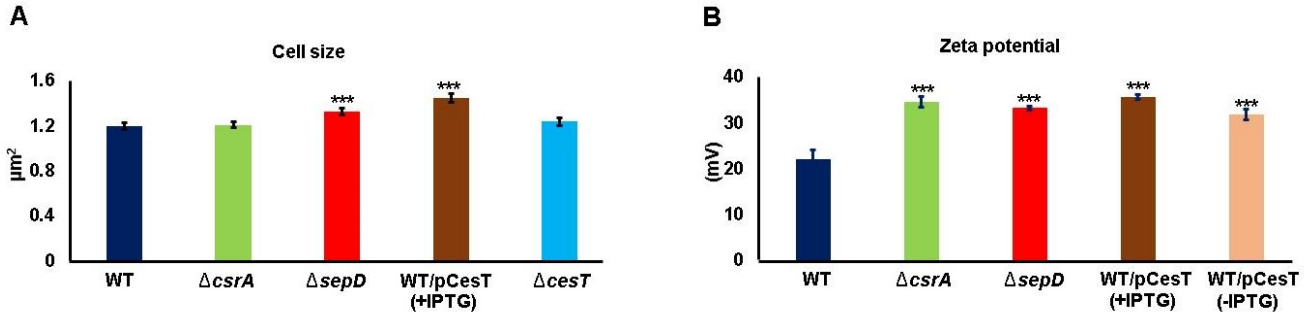

Figure 7. Cell size and effective electric charge on the bacteria's surface increase upon T3SS activation. Indicated EPEC strains were subcultured in DMEM at 37˚C to an OD_{600} of 0.6 and visualized under a microscope, and their size was measured (A). Zeta potential was measured to evaluate effective electric charge on the bacteria's surface upon T3SS activation (B). Data are presented as mean ± SE. N=4 with ~150 bacteria. *, $p<0.05$; ***, $p<0.001$.

Discussion

Many studies demonstrate the impact of CsrA on *E. coli* physiology and metabolism, mostly in the laboratory K12 model strains (17, 19-22), and other *E. coli* isolates (23), including EPEC (24). Despite differences in experimental conditions, methodologies and the mutations used, the metabolic signatures deduced or found in the studies mentioned above are overall in agreement and concur with our data. However, our study elucidates a new aspect of the CsrA function that was previously overlooked. We show here the critical impact of T3SS regulation of CsrA in controlling *E. coli* lipid composition. Our results point to extensive shifts in lipid metabolism associated with T3SS activation and CsrA repression. The most notable shifts are remodeling PL metabolism, including a shift from PS to PEs and LPLs and PGs to CLs, and in terpenoid quinones metabolism, including a shift from menaquinones and ubiquinones towards the production of undecaprenyl lipids. The notable upregulation in the total phospholipid in EPEC could be related to the cell size of the bacterium. In conclusion, our data indicate that CsrA controls the production of key components involved in the biogenesis of the bacterial cell envelope.

An important motivation for carrying out this study was elucidating how the activation of the T3SS, followed by effector injection and intimate attachment to the host, would influence EPEC metabolism. We consider that EPEC Δ*csrA* mutant would only partially phenocopy the physiological state of attached EPEC. This is since this mutant shows reduced growth rate and in addition it may collect suppressor mutations. To better mimic T3SS activation upon host attachment, which is followed by a rise in the levels of free CesT and transient CsrA inhibition, we capitalized on engineered EPEC strains that transiently and partially inhibit CsrA (as in attached EPEC) and show a growth rate similar to that of the wild type EPEC in our experimental conditions. These strains include a ΔsepD mutant that constitutively secretes Tir and EPEC/pCesT that overexpres CesT upon induction with IPTG. Using these strains, we carried out an unbiased lipidomics study. Our results are well-aligned with Berndt and colleagues, who recently published Δ*csrA* transcript data of EPEC (24). However, some discrepancies exist: our lipidomics analysis points to higher levels of LPLs, whereas the data of Berndt et al. disagree with this premise. This discrepancy may reflect differences in experimental conditions used in the two studies. For example, we grew the bacteria statically in DMEM to OD_{600} 0.6, while Brendt et al. used modified

M9 medium and grew the bacteria to OD_{600} 1.0. Notably, the critical factor in selecting our growth conditions and the used mutant was mimicking infection conditions. In conclusion, our data suggest that host-attached EPEC bacteria experience a major shift in lipid metabolism.

Whether and how the observed metabolic/lipidomic shift contributes to host colonization are key questions that remain to be addressed in follow up studies. Of particular interest are the shifts we found in terpenoid quinones and PLs. Bacteria use terpenoids like undecaprenyl phosphate (Und-P) as lipid carriers to assemble numerous glycan polymers that comprise the bacterial envelope. In *E. coli*, Und-P is required for synthesizing peptidoglycan, O-antigen, and exopolysaccharides (28). Importantly, *idi* removal suppressed mutation in undecaprenyl pyrophosphate synthase (important for synthesizing undecaprenyl phosphate) (29). Our finding that the expression of both *idi* and *ispU* is higher in the mutant *sepD* and in the over-expressing CesT strains, suggests that attachment to the host cell EPEC may remodel its envelope structure. This notion is supported by the considerable increase in LPS O-antigen levels. The shift from PLs towards LPLs and cardiolipins, and the resulting decrease in PL content may decrease the integrity and increase the permeability of bacterial membrane. Moreover, in our hands, PL chain length was shorter in the *sepD* mutant and in EPEC/pCesT. The shorter chain length is expected to further increase membrane permeability. The decrease in DOU may moderate this change. Staining with FM™ 4-64FX indicated a lower binding to leaf of the plasma membrane in the mutant, further indicating the possible remodeling of phospholipids upon attachment to host cell. Our analysis also show an increase in the levels of LPS in *sepD* and in the over-expressing CesT strains. Our analysis points to a considerable increase in the abundance of LPLs and LPAs, under conditions that mimic EPEC attachment. Interestingly, LPLs produced by host intestinal cells induce a cAMP-dependent signaling pathway in infecting *Salmonella*, resulting in the production and secretion of active flagellin (30). Thus it would be interesting to test if bacteria might use self-produced LPLs as a second messenger. Alternatively, EPEC may produce the LPAs to manipulate host signaling since LPA is a potent agonist of a family of five G protein-coupled receptors (GPCRs) associated with G_i, $G_{12/13}$, G_q, and G_s, which activate a plethora of downstream signaling pathways including PI3K, Ras, Rho, PLC and adenylate cyclase (31-36). Moreover, the interaction of LPAs with GPCRs inhibits pro-inflammatory responses induced by lipopolysaccharide (LPS) (32-34, 37). Given the above, we speculate that LPL and LPA

production and secretion may contribute to the capacity of EPEC to evade detection by the host immune response.

In conclusion, our work provides a comprehensive view of the influence of T3SS activation and the subsequent CsrA repression on lipid metabolism and membrane biogenesis. Our data point to a surprising and dramatic remodeling of the EPEC lipidome upon host attachment and provide a better view of the metabolic aspects of the bacterial switch from the planktonic to the cell-adherent lifestyle. Notably, this study provides the community with extensive and rich resources that lay the foundation for follow up studies.

Methods

Bacteria cultures

Bacterial strains and plasmids used are presented in **Supplementary Table 2** and primers in **Supplementary Table 3**. Bacteria were grown in Luria-Bertani (LB) broth supplemented, when needed, with ampicillin (100 µg/mL), streptomycin (50 µg/mL), chloramphenicol (25 µg/mL), kanamycin (Kan, 30 µg/mL), or tetracycline (10 µg/mL). For metabolite/lipid extraction EPEC were grown statically at 37˚C overnight in LB medium with respective antibiotics. The overnight grown bacterial cultures were then diluted 1:50 using high glucose Dulbecco's modified Eagle medium (DMEM; Biological Industries) lacking pyruvate and glutamate, and statically grown at 37˚C. To express CesT in strains containing the pCesT plasmid, 0.05 mM isopropyl-D-thiogalactopyranoside (IPTG) was added 3 h after culturing in DMEM. Bacterial growth was extended to 0.6 Abs at OD_{600}. The cells were then centrifuged (5000 g for 10 min at 4˚C), washed twice with 20 mL of cold phosphate-buffered saline (PBS), and pellets were immediately snap-frozen in liquid nitrogen.

Cloning, GFP fusion, and bacterial strain construction

For GFP fusion, bacteria were electroporated with pKD46 plasmid harboring λ Red genes (γ, β, and Exo) (38). The tet-sacB cassette (39) was introduced downstream to the desired gene of interest and replaced with GFP insertion. The primer sequence for GFP fusions is given as **(Supplementary Table 3)**. GFP fusions were verified using PCR with flanking primers. Primers for qRT-PCR confirmation of gfp fusions are shown in **Supplementary Table 4**. For overexpression of CesT levels, the pKD46 plasmids were cured, and pSA10 plasmid containing *CesT* was electroporated. Overexpression of CesT was induced upon IPTG induction.

Solvents for metabolomics and lipidomics analyses

Acetonitrile, methanol (both ultra-LC-MS grade), chloroform, and water (HPLC-MS grade) were supplied by JT Baker; isopropanol (HPLC-MS grade) from ChemSolute; and formic acid (HPLC-MS grade) by TCI. Ammonium fluoride (>99%) was supplied by Sigma-Aldrich. Internal standard EquiSPLASH LIPIDOMIX (MS-quantitative grade) mix was obtained from Avanti Polar Lipids, Inc.

Sample preparation for global metabolomics

Frozen pellets (45 mg) were reconstituted in 500 µL of acetonitrile: methanol: water (40:40:20) and transferred to pre-weighed clean tubes. For the extraction of metabolites, samples were subjected to five cycles of ultra-sonication (Bioruptor Plus; Diagenode, USA), each for 30 sec at 4˚C. Samples were then centrifuged at 13,000 g at 4˚C for 10 min, and the supernatant was transferred to clean tubes. The supernatant was concentrated in a vacuum concentrator (126 SC210A SpeedVac; Thermo Scientific) at 30˚C, and dry samples were reconstituted in 200 µL of acetonitrile/ methanol/ water 40:40:20. Samples were filtered through Acrodisc® PTFE membrane filters 0.2µm (Pall Corporation, USA) and transferred to HPLC tubes.

Sample preparation for lipidomics analyses

Bacteria (45 mg, wet pellet) were reconstituted in 400 µL of LC-MS grade water and transferred to glass tubes. Following the addition of 800 µL of ice-cold methanol, bacteria went through five cycles of 30-sec ultra-sonication at 4˚C for quenching and complete lysis. 400 µL of cold chloroform was added, and another sequence of 30-sec x 5 sonication cycles at 4°C was carried out. The tubes were incubated at room temperature for 30 min with occasional mixing (40) and then centrifuged at 770 g for 10 min at 4˚C for phase separation. The lower chloroform phase was

transferred to clean glass tubes, and the protein ring was re-extracted with the same solvent system. Protein ring extracts were then pooled with the respective sample. Samples were concentrated in vacuum and reconstituted in 200 µl 95 % acetonitrile, 0.1 FA.

UPLC-MS analysis

LC-MS analysis was carried out in a Waters Acquity UPLC H-Class (Waters, Milford, MA, USA) and Xevo X2-XS Q-ToF- High resolution, High Mass Accuracy Q-ToF (Waters, Manchester, UK) system. For the global metabolomics analysis, metabolites were separated on an Acquity UPLC®BEH amide column C18, 2.1 x 50 mm, 1.7 µm; waters, Ireland) column. A flow rate of 0.4 mL/min was used with a linear gradient, as shown in **Supplementary Table 5**. LC-MS runs for lipidomics analyses were performed using a UPLC CSH C18 column (100 mm × 2.1 mm, 1.7 µm; Waters). The column temperature was maintained at 60°C. The mobile phase consisted of 0.1% FA (vol/vol) in water (A), 0.1 FA in acetonitrile (B), and isopropanol (C). A flow rate of 0.4 mL/min was used with a linear gradient (**Supplementary Table 6**). ESI-MS was calibrated using sodium formate, and leucine enkephalin was used as the lock mass (m/z 556.2771, 200 pg/mL) and continuously infused at 6 µL/min. The capillary spray was maintained at 3.0 kV; the data were acquired in positive and negative mode with collision energies of 40-65 eV and 30-60 eV, respectively. Full-scan and MS^E data acquisition were performed, ranging from 30-2000 Dalton. Argon was used as the collision gas for collision-induced dissociation. The lock mass was continuously infused at 6 µL/min. MassLynx 4.1 (Waters Corporation, Milford, MA, USA) was used to control the instrument, calculate accurate masses, and mass spectral visualization. Ammonium fluoride was used for post-column derivatization to improve the yields of the neutral charged lipids in the ES+ mode.

Metabolomics and lipidomics analyses

Progenesis QI (Nonlinear Dynamics, Newcastle, United Kingdom) was used for spectra deconvolution, alignment, feature identification, and multivariate testing. Blank samples (solvents that went through the same sample preparation with no bacteria) were used to exclude artifactual mass features. Mass features eluted at t>1 minute, with minimum intensity higher than 100 m/z, with the lowest mean abundance in the blank, and fold change over 100 from blank, were used for analysis. Following quantile normalization, separation of the lipidome groups was visualized by principal component analysis (PCA) and heat maps using EZinfo 3.0 (Umetrics AB, Umea Sweden) and Metaboanalyst 4.0 (41). We repeated the quantification of PLs following normalization to internal standard (EquiSPLASH LIPIDOMIX). Full-scan and MS^E mass spectra were acquired from all masses of 30–2,000 Daltons. Identification of mass features was carried out using 18 metabolite libraries compatible with Progenesis QI and our internal library, based on mass accuracy < 5 ppm, isotope, fragmentation pattern, and elution time.

Data mining for gene expression and protein interactions with DNA

Changes in transcript levels mediated by CsrA (24) and CsrA-RNA interactions (17) were previously reported. We mined the publicly available databases that resulted from these studies for network-based analysis of lipid metabolism regulation by T3SS activation and CsrA inhibition. The list of enzymes involved in *E. coli* lipid synthesis was extracted from the KEGG database.

Determination of GFP fluorescence intensity

The strains with GFP fusion were grown overnight in LB containing chloramphenicol at 37˚C. The overnight cultures were subcultured (1:100) in DMEM high glucose medium. IPTG was added after 3 hours, and growth continued for an additional 3 hours. The cells were washed and suspended in PBS. The fluorescence of GFP was measured at 485 nm excitation and 510 nm emission using the Spark 10M microplate reader (Tecan Trading AG, Switzerland) and normalized to their respective optical densities (OD_{600}) (42).

Bacterial cell size and Zeta potential measurements

EPEC strains were subcultured in DMEM at 37˚C to an OD_{600} of 0.6. Bacteria were loaded on polylysine-coated glass slides; a coverslip was mounted on top, and the cells were visualized under a phase-contrast Axio Observer Z1 microscope (Zeiss, Germany). System control and image processing were performed with Zen pro-2012 (Zeiss, Germany). Bacterial cell size was measured using Image J software.

Zeta potential was measured as follows: Bacteria were centrifuged for 3 min at 16,000 g at 4˚C, washed and reconstituted with 1 mL of LCMS grade water. Zeta potential was determined using Zetasizer Nano ZS (Malvern Instruments, UK) at 25˚C. Zeta potential was calculated using the Smoluchowski model. Data acquisition from 15 events was recorded for every sample, and the average Zeta potential was determined from four replicates (43).

Membrane staining

For staining bacterial membranes, static cultures of EPEC strains were subcultured in DMEM at 37˚C to an OD_{600} of 0.6. The cells were washed with PBS, treated with 1 mg/mL FM4-64

(Molecular Probes, Invitrogen), and spotted on poly-L-lysine coated coverslips. Bacteria were visualized in an Eclipse Ti microscope (Nikon, Japan), equipped with a CoolSnap HQII camera (Photometrics, Roper Scientific, USA). System control, image processing, and fluorescence intensity measurement were performed with NIS Elements AR 4.3 (Nikon, Japan).

LPS Quantification

For staining bacterial O-antigen, static cultures of EPEC strains were subcultured in DMEM at 37˚C to an OD600 of 0.6. The cells were washed with PBS and spotted onto poly-L-Lysine coated coverslips. The cells on the coverslips were then fixed with 2% paraformaldehyde and 0.01% glutaraldehyde in sodium cacodylate buffer (0.1 M, pH 7.2) for 15 min at 25 C. Subsequently, coverslips were washed 3 times in PBS, incubated for 30 min with 2% BSA and then with rabbit anti-O127 antiserum, diluted 1:500 in PBS containing 2% BSA, for 1 hr at 25 C. Coverslips were then washed 3 times with PBS and incubated for 1 hr at 25 C with Alexa 488 conjugated goat anti-rabbit antibody, diluted 1:1000 in PBS. Coverslips were then washed 3 times with PBS and fixed with 2.5 % glutaraldehyde in sodium cacodylate buffer (0.1 M, pH 7.2) for 15 min at 25 C. The cells were visualized by Eclipse Ti microscope (Nikon, Japan), equipped with CoolSnap HQII camera (Photometrics, Roper Scientific, USA). System control, image processing and fluorescence intensity measurement were performed with NIS Elements AR 4.3 (Nikon, Japan).

Competing interests

We have no competing interests to report.

References

1. Nataro JP, Kaper JB. Diarrheagenic Escherichia coli. Clin Microbiol Rev. 1998;11(1):142-201.
2. Elliott SJ, Wainwright LA, McDaniel TK, Jarvis KG, Deng YK, Lai LC, et al. The complete sequence of the locus of enterocyte effacement (LEE) from enteropathogenic Escherichia coli E2348/69. Mol Microbiol. 1998;28(1):1-4.
3. Garmendia J, Frankel G, Crepin VF. Enteropathogenic and enterohemorrhagic Escherichia coli infections: translocation, translocation, translocation. Infect Immun. 2005;73(5):2573-85.
4. Gaytan MO, Martinez-Santos VI, Soto E, Gonzalez-Pedrajo B. Type Three Secretion System in Attaching and Effacing Pathogens. Front Cell Infect Microbiol. 2016;6:129.
5. Mellies JL, Elliott SJ, Sperandio V, Donnenberg MS, Kaper JB. The Per regulon of enteropathogenic Escherichia coli : identification of a regulatory cascade and a novel transcriptional activator, the locus of enterocyte effacement (LEE)-encoded regulator (Ler). Mol Microbiol. 1999;33(2):296-306.
6. Sanchez-SanMartin C, Bustamante VH, Calva E, Puente JL. Transcriptional regulation of the orf19 gene and the tir-cesT-eae operon of enteropathogenic Escherichia coli. J Bacteriol. 2001;183(9):2823-33.
7. Kenny B, DeVinney R, Stein M, Reinscheid DJ, Frey EA, Finlay BB. Enteropathogenic E. coli (EPEC) transfers its receptor for intimate adherence into mammalian cells. Cell. 1997;91(4):511-20.
8. Mills E, Baruch K, Aviv G, Nitzan M, Rosenshine I. Dynamics of the type III secretion system activity of enteropathogenic Escherichia coli. mBio. 2013;4(4).
9. Little DJ, Coombes BK. Molecular basis for CesT recognition of type III secretion effectors in enteropathogenic Escherichia coli. PLoS Pathog. 2018;14(8):e1007224.
10. Runte CS, Jain U, Getz LJ, Secord S, Kuwae A, Abe A, et al. Tandem tyrosine phosphosites in the Enteropathogenic Escherichia coli chaperone CesT are required for differential type III effector translocation and virulence. Mol Microbiol. 2018;108(5):536-50.
11. Lai Y, Rosenshine I, Leong JM, Frankel G. Intimate host attachment: enteropathogenic and enterohaemorrhagic Escherichia coli. Cell Microbiol. 2013;15(11):1796-808.

12. Login FH, Jensen HH, Pedersen GA, Amieva MR, Nejsum LN. The soluble extracellular domain of E-cadherin interferes with EPEC adherence via interaction with the Tir:intimin complex. FASEB J. 2018:fj201800651.

13. Katsowich N, Elbaz N, Pal RR, Mills E, Kobi S, Kahan T, et al. Host cell attachment elicits posttranscriptional regulation in infecting enteropathogenic bacteria. Science. 2017;355(6326):735-9.

14. Goddard PJ, Sanchez-Garrido J, Slater SL, Kalyan M, Ruano-Gallego D, Marches O, et al. Enteropathogenic Escherichia coli Stimulates Effector-Driven Rapid Caspase-4 Activation in Human Macrophages. Cell Rep. 2019;27(4):1008-17 e6.

15. Mills E, Baruch K, Charpentier X, Kobi S, Rosenshine I. Real-time analysis of effector translocation by the type III secretion system of enteropathogenic Escherichia coli. Cell Host Microbe. 2008;3(2):104-13.

16. Ye F, Yang FL, Yu RJ, Lin X, Qi JX, Chen ZJ, et al. Molecular basis of binding between the global post-transcriptional regulator CsrA and the T3SS chaperone CesT. Nature Communications. 2018;9.

17. Potts AH, Vakulskas CA, Pannuri A, Yakhnin H, Babitzke P, Romeo T. Global role of the bacterial post-transcriptional regulator CsrA revealed by integrated transcriptomics. Nat Commun. 2017;8(1):1596.

18. Romeo T, Gong M, Liu MY, Brun-Zinkernagel AM. Identification and molecular characterization of csrA, a pleiotropic gene from Escherichia coli that affects glycogen biosynthesis, gluconeogenesis, cell size, and surface properties. J Bacteriol. 1993;175(15):4744-55.

19. Sowa SW, Gelderman G, Leistra AN, Buvanendiran A, Lipp S, Pitaktong A, et al. Integrative FourD omics approach profiles the target network of the carbon storage regulatory system. Nucleic Acids Res. 2017;45(4):1673-86.

20. McKee AE, Rutherford BJ, Chivian DC, Baidoo EK, Juminaga D, Kuo D, et al. Manipulation of the carbon storage regulator system for metabolite remodeling and biofuel production in Escherichia coli. Microb Cell Fact. 2012;11:79.

21. Sabnis NA, Yang H, Romeo T. Pleiotropic regulation of central carbohydrate metabolism in Escherichia coli via the gene csrA. J Biol Chem. 1995;270(49):29096-104.

22. Suzuki K, Wang X, Weilbacher T, Pernestig AK, Melefors O, Georgellis D, et al. Regulatory circuitry of the CsrA/CsrB and BarA/UvrY systems of Escherichia coli. J Bacteriol. 2002;184(18):5130-40.

23. Revelles O, Millard P, Nougayrede JP, Dobrindt U, Oswald E, Letisse F, et al. The carbon storage regulator (Csr) system exerts a nutrient-specific control over central metabolism in Escherichia coli strain Nissle 1917. PLoS One. 2013;8(6):e66386.

24. Berndt V, Beckstette M, Volk M, Dersch P, Bronstrup M. Metabolome and transcriptome-wide effects of the carbon storage regulator A in enteropathogenic Escherichia coli. Sci Rep. 2019;9(1):138.

25. Deng W, Yu HB, Li Y, Finlay BB. SepD/SepL-dependent secretion signals of the type III secretion system translocator proteins in enteropathogenic Escherichia coli. J Bacteriol. 2015;197(7):1263-75.

26. Morin M, Ropers D, Letisse F, Laguerre S, Portais JC, Cocaign-Bousquet M, et al. The post-transcriptional regulatory system CSR controls the balance of metabolic pools in upper glycolysis of Escherichia coli. Mol Microbiol. 2016;100(4):686-700.

27. Nadeem MS, Razeeth M, Choudhry HMZ, Anwar F, Zamzami MA, Murtaza BN, et al. LC-MS/MS-based metabolic profiling of Escherichia coli under heterologous gene expression stress. J Cell Biochem. 2020;121(1):125-34.

28. Jorgenson MA, Young KD. Interrupting Biosynthesis of O Antigen or the Lipopolysaccharide Core Produces Morphological Defects in Escherichia coli by Sequestering Undecaprenyl Phosphate. J Bacteriol. 2016;198(22):3070-9.

29. MacCain WJ, Kannan S, Jameel DZ, Troutman JM, Young KD. A Defective Undecaprenyl Pyrophosphate Synthase Induces Growth and Morphological Defects That Are Suppressed by Mutations in the Isoprenoid Pathway of Escherichia coli. J Bacteriol. 2018;200(18).

30. Subramanian N, Qadri A. Lysophospholipid sensing triggers secretion of flagellin from pathogenic salmonella. Nat Immunol. 2006;7(6):583-9.

31. Chien HY, Lu CS, Chuang KH, Kao PH, Wu YL. Attenuation of LPS-induced cyclooxygenase-2 and inducible NO synthase expression by lysophosphatidic acid in macrophages. Innate Immun. 2015;21(6):635-46.

32. Zhao J, He D, Su Y, Berdyshev E, Chun J, Natarajan V, et al. Lysophosphatidic acid receptor 1 modulates lipopolysaccharide-induced inflammation in alveolar epithelial cells and murine lungs. Am J Physiol Lung Cell Mol Physiol. 2011;301(4):L547-56.

33. Fan H, Zingarelli B, Harris V, Tempel GE, Halushka PV, Cook JA. Lysophosphatidic acid inhibits bacterial endotoxin-induced pro-inflammatory response: potential anti-inflammatory signaling pathways. Mol Med. 2008;14(7-8):422-8.

34. Ciesielska A, Hromada-Judycka A, Ziemlinska E, Kwiatkowska K. Lysophosphatidic acid up-regulates IL-10 production to inhibit TNF-alpha synthesis in Mvarphis stimulated with LPS. J Leukoc Biol. 2019;106(6):1285-301.

35. Lin S, Han Y, Jenkin K, Lee SJ, Sasaki M, Klapproth JM, et al. Lysophosphatidic Acid Receptor 1 Is Important for Intestinal Epithelial Barrier Function and Susceptibility to Colitis. Am J Pathol. 2018;188(2):353-66.

36. Wiedmaier N, Muller S, Koberle M, Manncke B, Krejci J, Autenrieth IB, et al. Bacteria induce CTGF and CYR61 expression in epithelial cells in a lysophosphatidic acid receptor-dependent manner. Int J Med Microbiol. 2008;298(3-4):231-43.

37. Tsai HC, Han MH. Sphingosine-1-Phosphate (S1P) and S1P Signaling Pathway: Therapeutic Targets in Autoimmunity and Inflammation. Drugs. 2016;76(11):1067-79.

38. Datsenko KA, Wanner BL. One-step inactivation of chromosomal genes in Escherichia coli K-12 using PCR products. Proc Natl Acad Sci U S A. 2000;97(12):6640-5.

39. Li XT, Thomason LC, Sawitzke JA, Costantino N, Court DL. Positive and negative selection using the tetA-sacB cassette: recombineering and P1 transduction in Escherichia coli. Nucleic Acids Res. 2013;41(22):e204.

40. Rowlett VW, Mallampalli V, Karlstaedt A, Dowhan W, Taegtmeyer H, Margolin W, et al. Impact of Membrane Phospholipid Alterations in Escherichia coli on Cellular Function and Bacterial Stress Adaptation. J Bacteriol. 2017;199(13).

41. Chong J, Soufan O, Li C, Caraus I, Li S, Bourque G, et al. MetaboAnalyst 4.0: towards more transparent and integrative metabolomics analysis. Nucleic Acids Res. 2018;46(W1):W486-W94.

42. Elbaz N, Socol Y, Katsowich N, Rosenshine I. Control of Type III Secretion System Effector/Chaperone Ratio Fosters Pathogen Adaptation to Host-Adherent Lifestyle. mBio. 2019;10(5).

43. Wyness AJ, Paterson DM, Defew EC, Stutter MI, Avery LM. The role of zeta potential in the adhesion of E. coli to suspended intertidal sediments. Water Res. 2018;142:159-66.